



Sensitive magnetometry reveals inhomogeneities in charge storage and weak transient internal currents in Li-ion cells

Yinan Hu^{a,b,1}, Geoffrey Z. Iwata^{a,b,1,2}, Mohaddese Mohammadi^c, Emilia V. Silletta^c, Arne Wickenbrock^{a,b}, John W. Blanchard^b, Dmitry Budker^{a,b,d}, and Alexej Jerschow^{c,2}

^aInstitut für Physik, Johannes Gutenberg-Universität Mainz, 55099 Mainz, Germany; ^bHelmholtz Institute Mainz, GSI Helmholtzzentrum für Schwerionenforschung, 55099 Mainz, Germany ^cDepartment of Chemistry, New York University, New York, NY 10003; and ^dDepartment of Physics, University of California, Berkeley, CA 94720

Edited by Karl T. Mueller, Pacific Northwest National Laboratory, and accepted by Editorial Board Member Angela M. Gronenborn March 23, 2020 (received for review October 4, 2019)

The ever-increasing demand for high-capacity rechargeable batteries highlights the need for sensitive and accurate diagnostic technology for determining the state of a cell, for identifying and localizing defects, and for sensing capacity loss mechanisms. Here, we leverage atomic magnetometry to map the weak induced magnetic fields around Li-ion battery cells in a magnetically shielded environment. The ability to rapidly measure cells nondestructively allows testing even commercial cells in their actual operating conditions, as a function of state of charge. These measurements provide maps of the magnetic susceptibility of the cell, which follow trends characteristic for the battery materials under study upon discharge. In particular, hot spots of charge storage are identified. In addition, the measurements reveal the capability to measure transient internal current effects, at a level of μA , which are shown to be dependent upon the state of charge. These effects highlight noncontact battery characterization opportunities. The diagnostic power of this technique could be used for the assessment of cells in research, quality control, or during operation, and could help uncover details of charge storage and failure processes in cells.

magnetometry | battery diagnostics | optically pumped magnetometer | magnetic susceptibility

Rechargeable batteries lie at the heart of technological developments, enabling the use of renewable energy sources, powering electric vehicles, cell phones, and other portable electronics (1). Key to the success of many rechargeable battery-powered developments is the reliable fabrication and deployment of battery cells with sufficient capacities and lifetimes. One of the biggest challenges in this process, however, is to determine the quality of cells by nondestructive measurements. Currently used techniques which can give *in situ/operando* information include synchrotron-based scanning transmission X-ray microscopy (2), X-ray microdiffraction (3), and neutron diffraction and Raman spectroscopy (4). Manufacturers typically perform electrochemical testing and limited two-dimensional (2D) X-ray scanning (5, 6). X-ray tomography is a potentially powerful tool as well for commercial cells but is generally too slow for high-throughput use (5, 7). Ultrasound-based measurements are promising for characterization of cells based on changes in density and mechanical properties (8, 9).

Critical device parameters often elude many such examinations. In particular, once cells are compromised by mechanical impact, overcharging, or otherwise reaching their end of life, it is particularly difficult to investigate the causes and the propagation of failure modes (10). Destructive analysis can provide important clues, but materials can be significantly altered in the process. Furthermore, this approach precludes a study of cells over time and does not give access to markers for cell lifetimes (11). As a result, there is a pressing need for a high-throughput,

noncontact, diagnostic technique that can be deployed in any stage of battery production or life cycle.

Recently, it was demonstrated that magnetic susceptibility changes within cells could be measured nondestructively using an inside-out MRI (ioMRI) technique (12–14) that used the ^1H nuclear spin resonance frequencies in water to measure the susceptibility-induced field surrounding a cell when placed in a strong magnetic field. It was shown that the changes in the magnetic susceptibility could be tracked across the charge–discharge cycle, and that these changes followed the expected trends of the lithiation state of the cathode material. This approach thus provided a single-point state of charge measurement and allowed for the identification of inhomogeneities or non-idealities of charge storage in electrochemical cells. The ioMRI measurement is fast and provides high resolution but relies on

Significance

A long-standing challenge in battery research and development is the difficulty diagnosing commercial-type cell designs in their target form factors. The presented work significantly advances battery diagnostic techniques by establishing a contactless method using highly sensitive atomic magnetometers to directly measure and map a battery's induced magnetic field. The technique could provide detailed spatial information about the battery state, and possible internal defects and damage, without compromising the battery. We present findings of persistent, long-term internal currents within the battery, highlighting diagnostic tools afforded by the sensitivity of atomic magnetometers. The system allows fast measurements and would be implementable in a cost-effective, scalable manner. The measurement capabilities could be of significant interest to academic battery research and industry.

Author contributions: Y.H., G.Z.I., J.W.B., D.B., and A.J. designed research; Y.H. and G.Z.I. performed research; M.M., E.V.S., A.W., and A.J. contributed new reagents/analytic tools; Y.H., G.Z.I., M.M., E.V.S., and A.J. analyzed data; A.W., J.W.B., and D.B. supervised and advised the experiments; and G.Z.I. and A.J. wrote the paper.

Competing interest statement: The authors have filed a US provisional patent: Application number 62838909, EFS ID: 35838262, "System and method for magnetic susceptometry of devices with magnetometry."

This article is a PNAS Direct Submission. K.T.M. is a guest editor invited by the Editorial Board.

Published under the [PNAS license](#).

Data deposition: Data have been deposited in the Open Science Framework public repository at <https://osf.io/cw8zv/>, DOI: [10.17605/OSF.IO/CW8ZV](https://doi.org/10.17605/OSF.IO/CW8ZV).

¹Y.H. and G.Z.I. contributed equally to this work.

²To whom correspondence may be addressed. Email: iwata@uni-mainz.de or alexej.jerschow@nyu.edu.

This article contains supporting information online at <https://www.pnas.org/lookup/suppl/doi:10.1073/pnas.1917172117/-DCSupplemental>.

complex and costly MRI instrumentation. Moreover, while ioMRI is capable of mapping the charge distribution inside a cell, it is currently unable to distinguish between internal currents and induced effects (the magnetic field cannot easily be turned off), and lacks the sensitivity to detect tiny persistent internal currents (at the level of nA - μ A) that occur after charging or discharging.

In this work, we demonstrate the use of atomic magnetometers to enable mapping of the magnetic susceptibility within cells, and to report on the localized state of charge and the defects inside. While magnetometry has been used in the battery field for the study of the magnetic properties of active materials, powders or crystals (15, 16), this type of measurement has not been possible before for fully functioning macroscopic devices and form factors, operating under standard conditions. It is known that many battery material problems arise when upscaling from small cells to intermediate pouch cell designs, and hence it is critical to be able to diagnose internal characteristics of devices under realistic operating conditions, as many materials properties can change fundamentally in such situations. Therefore, the measurement technique demonstrated here provides information which, at the moment, cannot be obtained in any other way. With this technique, hotspots in charge storage can be identified within cells. Furthermore, the use of these sensors allows the measurement of tiny transient internal currents following cell discharge. These currents are shown to be particularly pronounced in the region of overdischarge.

Magnetic susceptibility measurements involve placing a sample in a magnetic field and measuring the smaller induced magnetic fields. At the same time, the magnetic field sensors, which typically have a limited dynamic range, need to be located in a small magnetic field (<50 nT) in order to detect the minute fields (<100 pT) induced by the cell.

The strategy employed in this work was to use a long flat solenoid to apply a magnetic field to the cell, as shown in Fig. 1.

The solenoid pierced a magnetically shielded region produced by concentric cylinders of mu-metal (17–19). In this arrangement, a negligible magnetic field is produced outside of the solenoid. The magnetic field sensors are placed in this region of negligible field within the magnetic shield and operate within their dynamic range (Fig. 1A). The induced magnetic field of a battery cell located inside the solenoid, however, is communicated to the sensor region without impediment. In addition to reducing environmental magnetic fields, the magnetic shield arrangement (Fig. 1B) also ensures that the magnetic flux lines emerging from the ends of the solenoid connect outside of the shielded region.

Atomic magnetometers were selected as the field sensors for this study because they offer the highest sensitivity, and simultaneous multiaxis measurements. These sensors provide a measure of the magnetic field via optical detection of the atomic electron resonance frequency shifts (20). Recently, atomic magnetometers have become commercially available in miniaturized designs (21). To obtain a magnetic field map of a battery, the cell is moved via a “conveyor belt” within the solenoid (Fig. 1B). The belt moves the battery past the sensors for scanning along the z coordinate. For subsequent scans, the cell was translated along x for the next scan while it was transported back to the original z position. In this way, the induced field from the battery was scanned across a rectangular area above and below the cell. Fig. 1C shows representative field maps for the magnetic field components, B_x and B_z , obtained from a single sensor above the battery. These maps, recorded with the solenoid turned on, are consistent with maps expected for a rectangular block with approximately uniform susceptibility (similar to a dipole field map), which represents a good first approximation of a cell. Fig. 1D shows the circuit setup for switching between the charge and discharge operation of the cell. The cell was connected to this circuit via twisted wires running along the conveyor belt.

Without the solenoid field applied to the battery, the setup is solely sensitive to internal currents within the battery, and any

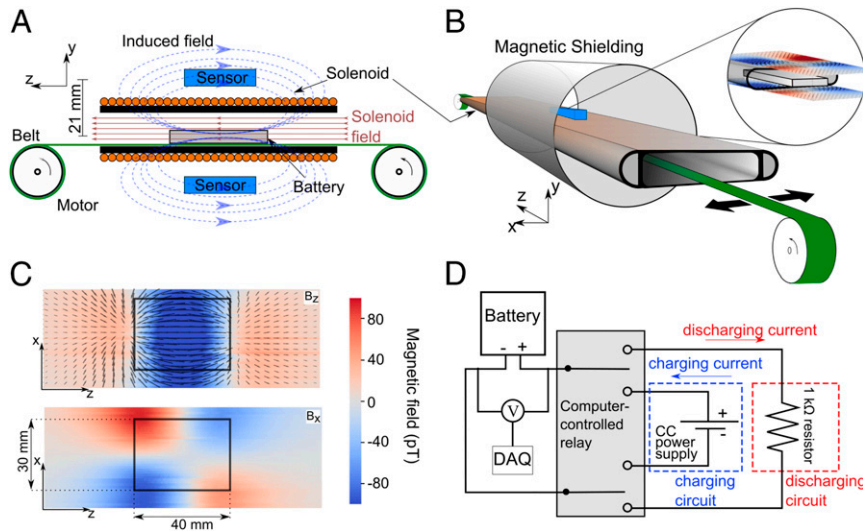


Fig. 1. Experimental susceptometry setup. (A) Side view of the experimental arrangement. A battery is placed on a motor-driven “conveyor belt” that moves the cell through a custom-designed solenoid, which provides a constant internal magnetic field. Magnetic field sensors are placed in the ultralow-field region, above and below the solenoid. (B) Three-dimensional drawing of the experimental arrangement. The solenoid is shown extending beyond the Twinleaf MS-2 magnetic shielding (only the innermost shield is shown—a total of four concentric cylinders were used). The conveyor belt moves the battery back and forth along the z axis, while translation stages on each end move the entire belt with 0.1-mm precision along the x axis. (Inset) Illustration of the location of the resulting 2D field maps acquired by this setup. (C) Sample-induced magnetic field map for a healthy battery charged to 90% capacity, obtained from a single sensor 21 mm above the battery. (Upper) Color map of the z component of the measured field, with an overlaid vector map of the total field in the x - z sensor plane. (Lower) The x -component color map of the measured field. The battery outline is shown as a black rectangle. (D) Circuit diagram for charging and discharging. The computer-controlled relay disconnects the battery cell from the charging/discharging circuits during measurements. However, the DAQ unit remained connected throughout the measurement. V: Voltmeter. CC: constant current.

remnant magnetization of the battery components. Turning on the solenoid field induces a magnetization within the cell, dependent on the local magnetic susceptibility. This magnetization produces a field that is detected by the magnetometers.

Results and Discussion

Identification of Internal Currents after Discharge. To measure a battery's magnetic properties across a discharge cycle, the behavior of the cell voltage and the induced magnetic field were monitored during 30-min rest periods between 30-min discharge periods. For discharge, the battery electrodes were connected to a 1-k Ω resistor, as shown in Fig. 1D. The solenoid field was on during this measurement, so the apparatus was sensitive to susceptibility-induced fields.

As is documented in the literature, long-term continuous discharging of the battery followed by a disconnection of the terminals leads to a "recovery effect," where the battery voltage relaxes to a higher equilibrium voltage level over a period of time (22, 23). The magnetic sensors recorded transient fields that we associate with this voltage increase based upon the well-matched long-term time constants of the exponential relaxation to a steady-state value.

Fig. 2A shows a series of 30-min magnetic field measurements during the rest periods immediately after disconnecting the cell from the discharge circuit. The magnetic field values are referenced to the open-cell voltage, OCV = 0 V (813-mAh depth of discharge), extrapolated from the behavior in the overdischarge regime. Transient magnetic fields were observed, which relaxed

exponentially toward a steady-state value. The signal immediately following each period of discharge was fit to a single exponential function of the form $y(x) = Ae^{-x/t_1} + c$, where A is the amplitude of the fit function, t_1 is the time constant, and c is an offset representative of the long-term static value. The time constants were stable with an average of 11 ± 4 s in the "healthy" battery regime up to its rated capacity (600 mAh). By contrast, the time constant increased significantly to 400–750 s when discharging beyond this region. The region of overdischarge is represented by shaded regions in Fig. 2. Red squares in Fig. 2A indicate the fitted time constants of the transient fields. The long-term static value of the magnetic field, c , decreased to background levels when the solenoid field was turned off. Therefore, this value must reflect the fields generated by the induced magnetic field, and specifically relate to the magnetic susceptibility of the battery components. The transient fields are present even when the solenoid is turned off, which provides corroboration that they are not due to susceptibility changes in the cell. Instead, they appear to be related to internal equilibration currents, which are likely related to the concentration gradient-driven diffusion of active materials in the battery (23, 24). In the overdischarge region, these currents may be exacerbated as a result of accelerated self-discharge due to corrosion of the copper current collector in the electrolyte (25). These degenerative effects, however, are not well-characterized at this point, nor does there appear to be a straightforward experimental technique to identify their origin (26).

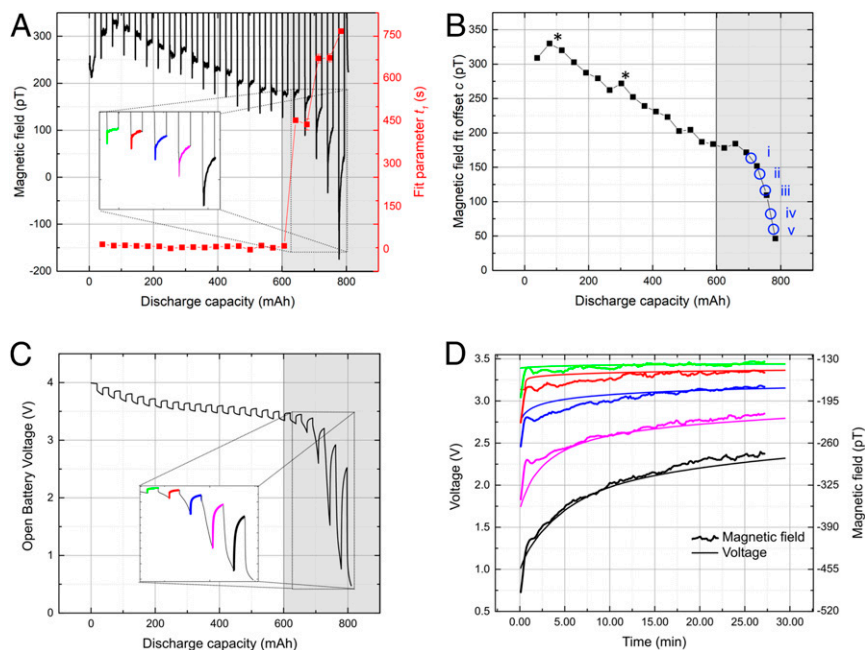


Fig. 2. Magnetic field and voltage response of a cell after discharging. Magnetic field measurements above the cell at a location corresponding to the upper-left corner of the battery outline in Fig. 1C, and voltage measurements as a function of discharge capacity. The shaded areas indicate the overdischarge region, when the battery was measured after being discharged beyond its rated capacity (600 mAh). (A) Magnetic field, B_x , measured with an atomic magnetometer for periods of 30 min at the indicated discharge capacity, beginning immediately after disconnecting the discharge circuit (see *Methods* for details). (Inset) Detail of the magnetic field decay for discharge capacities beyond the battery rating, where the equilibration time to a steady-state value increases, suggesting the presence of persistent internal currents within the cell. Red squares indicate the fitted time constants of the exponential behavior within each measurement period. Magnetic field values are referenced to a value extrapolated to the full discharge capacity of cell (OCV = 0 V, 813 mAh). (B) Steady-state magnetic field values determined by fitting the 30-min measurement curves in A to an exponential decay. The field amplitude exhibits a gradual decrease until reaching the rated capacity and a steeper falloff in the shaded region. Roman numerals indicate the points at which the magnetic field maps of Fig. 3A were acquired. Asterisks mark data points which were acquired during large environmental field fluctuations as assessed by an independent fluxgate measurement. (C) Voltage vs. discharge capacity. During the discharge periods, the measured voltage drops and then recovers when the battery is disconnected from the discharge circuit. (Inset) Detail of the voltage signal decay for discharge capacities beyond the battery rating. (D) Detail of the signal decay for discharge capacities beyond the battery rating (600 mAh). The colors correspond to those used in the insets in A and B.

Fig. 2B shows that the long-term static values of the magnetic field after each discharge period exhibit a linear dependence on the depth of discharge. This relationship between the battery's state of charge and the measured induced magnetic field, and by extension, the magnetic susceptibility, provides a noncontact alternative to voltage measurements for battery diagnostics. The features at 90 and 300 mAh can be attributed to laboratory noise that occurred during the measurement, as assessed by independent fluxgate field measurements outside the shield in the vicinity of the setup (marked with an asterisk in the figure). Within the healthy range (up to the rated capacity), the long-term field value changes gradually; beyond the rated discharge capacity (in the shaded region), we observe a significantly stronger effect. This behavior is in line with previous observations for these types of cells with cathode material containing a large amount of cobalt, and can be related to the change of the magnetic susceptibility over the course of discharge (12). *SI Appendix* details the composition of the cell obtained via scanning electron microscopy (SEM) cross-sectioning and micro-analysis measurements in *SI Appendix, Figs. S1 and S2*, and in *SI Appendix, Table S1*.

We note here that ultrasound diagnostic measurements also provide a noncontact and nondestructive means of determining the state of charge of a battery cell. These acoustic techniques are particularly sensitive to the density distribution of graphite, which is correlated to its lithiation state (8, 9). But, they show generally little sensitivity to changes in the distribution of light battery components, as well as changes in the cathode, and do not have a means of reporting on internal cell currents.

Fig. 2C shows the voltage measurement during the same experiment for comparison. Voltage was measured both during the discharge and during the magnetic field measurement period, when the battery was not connected to the discharge resistor. Here, too, there is a clear long-term recovery period in the shaded region, which becomes stronger with depth of discharge. We found that the time constants for this voltage measurement and those of the magnetic field measurements agreed with each other (Fig. 2D) in the overdischarge region (shaded). This finding indicates that the measured internal currents are likely related to these relaxation effects. Notably, fitting voltage measurements during the relaxation period in both the healthy and overdischarge regimes required a double exponential, while the magnetic field measurements fit reliably well with a single time constant. This finding can likely be attributed to the influence of the connected circuitry on the voltage measurements. The relative amplitude of the two fit components in the double exponential can be compared to establish whether transient currents or the influence from the connected circuitry is dominant. Before reaching the rated discharge capacity, the overall timescale for the voltage to settle was more than an order of magnitude smaller than in the region of overdischarge. Details on fitting the voltage time constants are shown in *SI Appendix, Fig. S3*. This figure also illustrates the large uncertainties for the fast time constant obtained from the voltage measurements.

Battery capacity recovery effects have been explained through a variety of models, motivated by experimental data acquired via voltage measurements (24, 27). The magnetic field measurement, by contrast, provides a contactless measure of the internal current effects and therefore enables a measurement that is decoupled from the electrical circuit, in addition to providing spatial resolution. As a result, future battery diagnostics using these magnetic field measurements could shed light onto the validity of these models, especially since they would also provide a spatially localized map of current behavior. Given the achieved measurement sensitivity (~ 10 pT $\sqrt{\text{Hz}}$), transient internal currents as small as ~ 4 μA can be sensed with this setup. These measurements do not require the solenoid and can in principle

be performed in a fully closed shield, in which the magnetometers can achieve a sensitivity of 20 fT/ $\sqrt{\text{Hz}}$. In such an arrangement the current sensitivity could approach 8 nA.

Measurements of Magnetic Susceptibility Maps. The relationship between the battery's state of charge and the magnetic susceptibility has been established in previous work using ioMRI (12). During battery charging and discharging, the amount of lithium distributed between anode and cathode alters the electronic configuration of the battery materials, leading to changes in magnetic susceptibility. This relationship has been carefully studied in controlled experiments on isolated electrode materials (16, 28–31). In a complete cell, susceptibility changes are a cumulative effect from different battery components arising from different phenomena and of different magnitude, and the ioMRI approach has shown that such changes could be observed across the charge cycle in fully operating cells (12).

The magnetometry approach taken herein provides a number of opportunities for the detection and characterization of magnetic susceptibility distributions within cells, including the ability to measure at lower magnetic fields, to separate the susceptibility effects from current effects, and to measure several field components at once. Fig. 3A shows a series of 2D maps of magnetic field measurements after cell equilibration at the discharge values indicated in Fig. 2B. It is again observed that the overall magnetic field decreases with discharge. Furthermore, a regularized magnetic field inversion produces magnetic susceptibility maps for each.

It is observed that the magnetic susceptibility, and hence the charge, is distributed nonuniformly across the cell, which could be due to the position of the battery tabs and other internal geometrical and material arrangements. Even though the overall susceptibility decreases, the main feature of two maxima in the distribution appears to persist through the continued discharge. The positive values for susceptibility indicate overall a paramagnetic behavior of the battery cell.

The sensitivity of the magnetic field measurements would also allow the identification of defects in cells by identifying deviations from the norm in the distribution of the magnetic susceptibility, or by simply using the field measurements for cell classification. In *SI Appendix* we show changes in observed magnetic field maps due to physical impact, although more comprehensive and controlled studies would have to be made to make direct links between measurements and defect types.

Alternative Sensors and Configurations. Similar measurements could, in principle, be performed with other magnetometer sensor technologies. In particular, suitable candidate sensors for efficient measurement include various types of atomic magnetometers (20), magnetometers based on nitrogen-vacancy (NV) centers in diamond (32), Hall probes (33), magnetoresistive sensors (34), superconducting quantum interference devices (SQUIDs) (35), and fluxgates. NV magnetometers and magnetoresistive sensors, for example, would offer a relatively high sensitivity over a large dynamic range, useful for batteries containing magnetic materials or those which exhibit large changes in susceptibility as they are charged or discharged (36). Furthermore, the small size of these sensors could allow for a higher spatial resolution measurement of the induced magnetic field. These can be used in a sensor array to reduce the mapping time, depending on the minimal stand-off distance of the sensor. Since microwaves that are typically used in NV measurements may be undesirable in some applications, recently developed microwave-free NV sensing protocols could be deployed in this case (37). In addition, a microwave-free sensing protocol and a diamond magnetometer have been used to create conductivity maps of conductive objects with submillimeter spatial resolution (38) in a substantial background field up to 100 mT. This procedure could

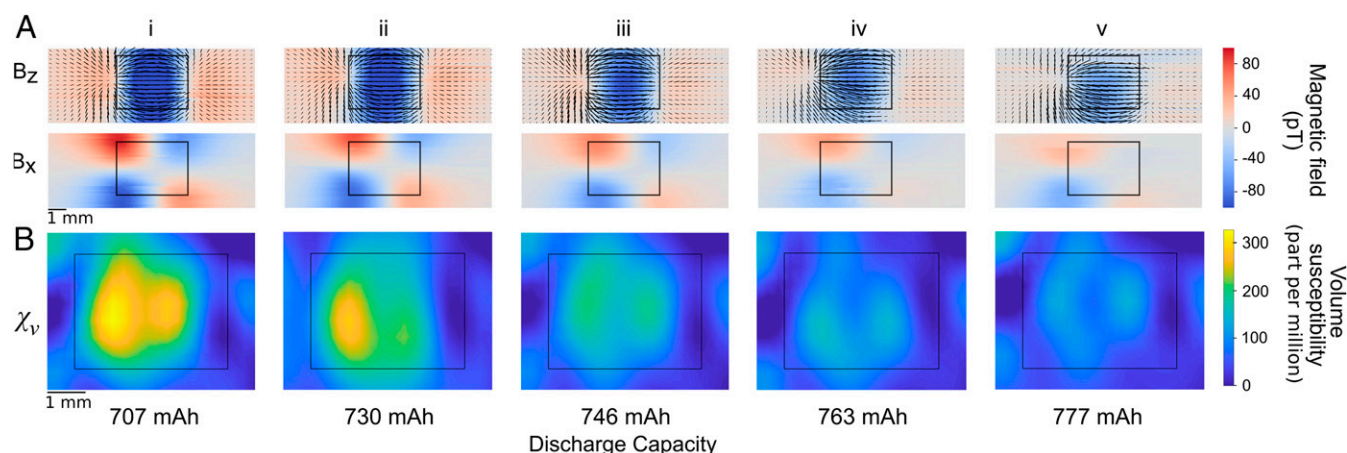


Fig. 3. Magnetic field and corresponding susceptibility maps above a cell. Roman numerals relate these selected snapshots to the points along the discharge curve in Fig. 2B. The corresponding discharge capacity is given at the bottom. (A, Upper) Field map in the z direction, with an x - z field vector map overlaid. (A, Lower) Field in the x direction. The black rectangular outline represents the battery position. Battery leads (not indicated) are to the left of the black rectangle. (B) Two-dimensional magnetic susceptibility maps (indicated in parts per million [ppm]) obtained from a regularized inversion of the measured magnetic field.

be easily adapted to alternating-current magnetic susceptibility measurements as well. Fluxgate sensors also offer ease of use and low cost but have lower sensitivity and poor spatial resolution. For sensors with a dynamic range that can accommodate environmental noise, it would be possible to lower the magnetic shielding demands by, for example, compensating this noise using an array of background sensors.

The induced field amplitude is proportional to the field produced by the solenoid; therefore, the measurement of the magnetic susceptibility distribution could be made more sensitive by increasing the solenoid field. In addition, varying or modulating the magnetic field of the solenoid would also provide further means of separating the effects of magnetic susceptibility and internal currents.

The sensor arrangement shown is currently limited to two-axes field measurements, but a three-axes arrangement could be implemented with sensor arrays.

Conclusion

We have demonstrated the ability to detect changes in magnetic susceptibility distributions in rechargeable battery cells by measuring the small induced magnetic fields around battery cells with atomic magnetometers. These measured fields are further shown to correlate with the state of charge of the cell. In addition, magnetic fields produced by weak transient internal currents have been detected with the same approach. In the overdischarge region the marked lengthening of the current relaxation timescales was observed. These measurements can be performed *in situ* and *operando* in realistic cells of commercial-type design under standard conditions. Magnetic shielding and a solenoid were arranged in such a way that the sensors did not directly measure the magnetic field produced by the solenoid, while retaining full sensitivity to the fields originating from and induced within the battery. These measurement observables provide hitherto inaccessible opportunities for cell characterization, classification, and monitoring. The approach and method are in principle scalable and could be adapted to measure large-format cells as well, as used, for example, in electric vehicles. This diagnostic technique could be used across all stages of battery cell research, production, and deployment.

Methods

Battery Cells. Measurements were performed on Li-ion pouch cells (Powerstream PGE8NMU53040) with dimensions of $\sim 2.9 \times 3.9 \times 0.7$ cm³. Each cell

has 12 pairs of active electrodes arranged in a flattened jelly-roll configuration. The anode consists of graphite on a copper current collector and the cathode consists of nickel manganese cobalt oxide on an aluminum current collector. Energy-dispersive X-ray spectroscopy of the cathode materials revealed the composition as 44.25% Co, 33.20% O, 3.11% Mn, 13.95% C, 5.04% Ni, 0.1% Ti, and 0.24% P in weight percentage. *SI Appendix, Figs. S1 and S2 and Table S1* summarize the detailed measurement results. The separator material is polyolefin. SEM images of battery components (including cross-sections for the electrode layers) are shown in *SI Appendix*.

The magnetic field around each battery with the solenoid off was measured to be less than 20 pT in any direction before performing experiments. This field (due to remnant magnetization) was mapped for each cell with the solenoid field off and subtracted from the induced field maps.

Solenoid, Magnetic Shield, Magnetometers, and Data Acquisition. All measurements were performed inside a Twinleaf M5-2 magnetic shield, operated with endcaps removed. The magnetic shield had four cylindrical layers of mu-metal shielding material with the innermost shield diameter of 180 mm and the outermost shield diameter of 304.5 mm. The overall length of the outermost shield was 620 mm. At the center of the shield cylinders, the laboratory magnetic fields were reduced by a factor of 10^4 in the direction parallel to the cylinder axis, and 10^5 in the transverse direction.

With endcaps removed and compensation fields applied, the magnetic field on top and below the center of the solenoid within the magnetic shield region was measured to be below 10 pT. This value was well within acceptable background levels for the susceptibility measurements. Acquiring measurements within an open shield reduces baseline noise in the magnetometer to environmental noise-dominated ~ 40 pT/ $\sqrt{\text{Hz}}$ in the x direction and ~ 200 pT/ $\sqrt{\text{Hz}}$ in the z direction (larger due to open-cylinder arrangement), within the sensor bandwidth of 0 to 150 Hz. The measurement can be susceptible to large transient magnetic artifacts and long-term drifts resulting from other equipment in the laboratory or in the building; therefore, the background fields were monitored using a fluxgate magnetometer to ensure that measurements were not taken during large background-field fluctuations.

The coil was fabricated with 3,560 turns of 0.56-mm-diameter wire and uniform spacing on a 1-m-long aluminum mount. *SI Appendix, Fig. S5* shows the cross-section of the flat solenoid design as well as a picture of the solenoid itself. A current of 3 mA was fed through the coil to produce a field of 2×10^{-5} T at the center of the coil, measured using a small-sized fluxgate sensor. Two QuSpin zero-field rubidium-vapor spin-exchange relaxation free magnetometers (21) (generation 1) were used (36). Each sensor was placed 2 cm above or below the center of the solenoid. Only the data from a single sensor are required for all of the measurements shown in this work, and the second sensor was included for redundancy.

To measure the discharge behavior of the cell, it was discharged by drawing 2–3 mA of current over a 1-k Ω resistor for 30 min at a time. The cell was subsequently disconnected from the resistor for a further 30 min.

During this rest period, the magnetic field at a single point above the battery was measured continuously. The position of the sensor for these measurements was determined by choosing a maximum point in the magnetic field map (upper-left corner of the battery in Fig. 1C). An analog input channel of a data acquisition (DAQ) unit was connected to the circuit during both discharging and rest conditions. These discharge and rest cycles were repeated over 24 h. During this periodic discharge measurement, the solenoid field was on, so that susceptibility changes could be monitored. The same measurement performed with the solenoid field off yielded no induced field in the cell, and the relaxation time constants for internal currents were determined to be similar as when the solenoid field was turned on. The discharge capacity of the battery at each point was determined by taking the average current measured in the discharge circuit during a discharge period, multiplied by the discharge time.

The cell was transported through the solenoid region and past the sensors using a conveyor belt made of vinyl tape, chosen for its low-friction backing and its nonmagnetic properties. The belt was moved via servo motors that were placed outside the shielded region. Each servo motor was mounted on a translation stage (Thorlabs KMTS50E/M). This arrangement allowed the entire belt to move in the x direction with 0.1-mm precision, enabling scanning measurements of the batteries. The sensors measured the x - and z magnetic field components in a plane parallel to the battery (Fig. 1).

The QuSpin electronics provide dedicated analog voltage output channels corresponding to the measured magnetic field in the x - or z directions (21). These voltages were measured using a National Instruments DAQ (NI-9205). The motion of the conveyor belt was controlled via a custom Python program that sequentially moved the belt forward by ~ 40 cm and was then reset to the original longitudinal position while the translation stages laterally moved the belt by 0.5 mm for the next scan. The DAQ was triggered by a mechanical switch that was tripped at the end of the conveyor belt reset movement. Each map took ~ 15 min to acquire, limited by the speed of

the motors used, and was obtained using an average of six runs. The magnetic field data were filtered for line noise and harmonics and smoothed using a 20-point window.

The spatial resolution of the magnetic field at the sensor is limited by the size of the probe laser beam within the atomic magnetometer and is estimated to be a voxel of $\sim 2 \times 2 \times 2$ mm³. The temporal resolution for the sensor is 150 Hz.

For measurements of internal currents within the battery, the cell was positioned directly below the sample and data were taken continuously at a 1-kHz acquisition rate. The frequency response of the sensor, however, attenuates signals above 150 Hz.

Magnetic Field Inversion. Regularized magnetic field inversion was performed using a dipolar field kernel and a truncated singular-value decomposition (39). The volume magnetic susceptibility distribution was obtained as an average value across the thickness of the cell (y direction). Singular values of the dipolar kernel transformation matrix were truncated below a value of 5×10^{-7} T to achieve regularization and stability of the inversion. The resolution of the susceptibility map is estimated to be ~ 5 mm.

Data Availability. The data that support the findings of this study are available in the Open Science Framework public repository (40). The corresponding authors can provide analysis code upon reasonable request.

ACKNOWLEDGMENTS. The work was funded in part by a grant by the US National Science Foundation under Award CBET (Chemical, Bioengineering, Environmental and Transport systems) 1804723 and the German Federal Ministry of Education and Research within the Quantumtechnologien program (grant FKZ13N14439) and the Deutsche Forschungsgesellschaft (DFG) through the Deutsch-Israelische Partnerschaft (DIP) program (grant FO703/2-1).

1. M. Li, J. Lu, Z. Chen, K. Amine, 30 years of lithium-ion batteries. *Adv. Mater.* **30**, e1800561 (2018).
2. J. Lim *et al.*, Origin and hysteresis of lithium compositional spatiodynamics within battery primary particles. *Science* **353**, 566–571 (2016).
3. J. Liu, M. Kunz, K. Chen, N. Tamura, T. J. Richardson, Visualization of charge distribution in a lithium battery electrode. *J. Phys. Chem. Lett.* **1**, 2120–2123 (2010).
4. J.-C. Panitz, P. Novák, O. Haas, Raman microscopy applied to rechargeable lithium-ion cells—steps towards in situ Raman imaging with increased optical efficiency. *Appl. Spectrosc.* **55**, 1131–1137 (2001).
5. V. Wood, X-ray tomography for battery research and development. *Nat. Rev. Mater.* **3**, 293–295 (2018).
6. A. Väyrynen, J. Salminen, Lithium ion battery production. *J. Chem. Thermodyn.* **46**, 80–85 (2012).
7. V. Yufit *et al.*, Investigation of lithium-ion polymer battery cell failure using X-ray computed tomography. *Electrochem. Commun.* **13**, 608–610 (2011).
8. A. G. Hsieh *et al.*, Electrochemical-acoustic time of flight: In operando correlation of physical dynamics with battery charge and health. *Energy Environ. Sci.* **8**, 1569–1577 (2015).
9. G. Davies *et al.*, State of charge and state of health estimation using electrochemical acoustic time of flight analysis. *J. Electrochem. Soc.* **164**, A2746–A2755 (2017).
10. J. Zhang, J. Lee, A review on prognostics and health monitoring of Li-ion battery. *J. Power Sources* **196**, 6007–6014 (2011).
11. M. Broussely *et al.*, Aging mechanism in Li ion cells and calendar life predictions. *J. Power Sources* **97–98**, 13–21 (2001).
12. A. J. Ilott, M. Mohammadi, C. M. Schauerman, M. J. Ganter, A. Jerschow, Rechargeable lithium-ion cell state of charge and defect detection by in-situ inside-out magnetic resonance imaging. *Nat. Commun.* **9**, 1776 (2018).
13. K. Romanenko, A. Jerschow, Distortion-free inside-out imaging for rapid diagnostics of rechargeable Li-ion cells. *Proc. Natl. Acad. Sci. U.S.A.* **116**, 18783–18789 (2019).
14. M. Mohammadi, E. V. Sillelta, A. J. Ilott, A. Jerschow, Diagnosing current distributions in batteries with magnetic resonance imaging. *J. Magn. Reson.* **309**, 106601 (2019).
15. R. Würschum *et al.*, Defects and charging processes in Li-ion battery cathodes studied by operando magnetometry and positron annihilation. *Mater. Sci. Forum* **879**, 2125–2130 (2016).
16. G. Klinser *et al.*, Charging of lithium cobalt oxide battery cathodes studied by means of magnetometry. *Solid State Ion.* **293**, 64–71 (2016).
17. S. Xu, S. M. Rochester, V. V. Yashchuk, M. H. Donaldson, D. Budker, Construction and applications of an atomic magnetic gradiometer based on nonlinear magneto-optical rotation. *Rev. Sci. Instrum.* **77**, 083106 (2006).
18. S. Xu *et al.*, Magnetic resonance imaging with an optical atomic magnetometer. *Proc. Natl. Acad. Sci. U.S.A.* **103**, 12668–12671 (2006).
19. V. V. Yashchuk *et al.*, Hyperpolarized xenon nuclear spins detected by optical atomic magnetometry. *Phys. Rev. Lett.* **93**, 160801 (2004).
20. D. Budker, M. Romalis, Optical magnetometry. *Nat. Phys.* **3**, 227–234 (2007).
21. V. K. Shah, R. T. A. Wakai, A compact, high performance atomic magnetometer for biomedical applications. *Phys. Med. Biol.* **58**, 8153–8161 (2013).
22. S. Narayanaswamy *et al.*, On battery recovery effect in wireless sensor nodes. *ACM Trans. Des. Autom. Electron. Syst.* **21**, 1–28 (2016).
23. H. Arora, R. S. Sherratt, B. Janko, W. Harwin, Experimental validation of the recovery effect in batteries for wearable sensors and healthcare devices discovering the existence of hidden time constants. *J. Eng. (Stevenage)* **2017**, 548–556 (2017).
24. S. Park, A. Savvides, M. B. Srivastava, “Battery capacity measurement and analysis using lithium coin cell battery” in *ISLPED’01: Proceedings of the 2001 International Symposium on Low Power Electronics and Design*, (IEEE, 2001), pp. 382–387.
25. S.-T. Myung, Y. Hitoshi, Y.-K. Sun, Electrochemical behavior and passivation of current collectors in lithium-ion batteries. *J. Mater. Chem.* **21**, 9891–9911 (2011).
26. I. A. Shkrob, M.-T. F. Rodrigues, D. P. Abraham, Fast charging of Li-ion cells: Part III. Relaxation dynamics and trap-controlled lithium ion transport. *J. Electrochem. Soc.* **166**, A4168–A4174 (2019).
27. P. Rong, M. Pedram, Battery-aware power management based on Markovian decision processes. *IEEE Trans. Comput. Aided Des. Integrated Circ. Syst.* **25**, 1337–1349 (2006).
28. T. Kadyk, M. Eikerling, Magnetic susceptibility as a direct measure of oxidation state in LiFePO₄ batteries and cyclic water gas shift reactors. *Phys. Chem. Chem. Phys.* **17**, 19834–19843 (2015).
29. J. E. Greedan, N. P. Raju, I. J. Davidson, Long range and short range magnetic order in orthorhombic LiMnO₂. *J. Solid State Chem.* **128**, 209–214 (1997).
30. J. T. Hertz *et al.*, Magnetism and structure of LiCoO₂ and comparison to NaCoO₂. *Phys. Rev. B Condens. Matter Mater. Phys.* **77**, 075119 (2008).
31. N. A. Chernova *et al.*, Layered Li_xNi_yMn_{1-x-y}O₂ cathodes for lithium ion batteries: Understanding local structure via magnetic properties. *Chem. Mater.* **19**, 4682–4693 (2007).
32. J. M. Taylor *et al.*, High-sensitivity diamond magnetometer with nanoscale resolution. *Nat. Phys.* **7**, 270 (2011).
33. A. Grosz, M. J. Haji-Sheikh, S. C. Mukhopadhyay, *High Sensitivity Magnetometers* (Springer, 2016).
34. C. Dolabdjian, D. Ménard, “Giant Magneto-Impedance (GMI) magnetometers” in *High Sensitivity Magnetometers*, A. Grosz, M. J. Haji-Sheikh, S. C. Mukhopadhyay, Eds. (Springer International Publishing, 2017), pp. 103–126.
35. J. Clarke, “SQUID Fundamentals” in *SQUID Sensors: Fundamentals, Fabrication and Applications*, H. Weinstock, Ed. (Springer, Dordrecht, The Netherlands, 1996).
36. H. B. Dang, A. C. Maloof, M. V. Romalis, Ultrahigh sensitivity magnetic field and magnetization measurements with an atomic magnetometer. *Appl. Phys. Lett.* **97**, 151110 (2010).
37. A. Wickenbrock *et al.*, Microwave-free magnetometry with nitrogen-vacancy centers in diamond. *Appl. Phys. Lett.* **109**, 053505 (2016).
38. G. Chatzidrosos *et al.*, Eddy-current imaging with nitrogen-vacancy centers in diamond. *Phys. Rev. Appl.* **11**, 014060 (2019).
39. P. C. Hansen, J. G. Nagy, D. P. O’Leary, *Deblurring Images: Matrices, Spectra, and Filtering* (SIAM, 2006).
40. G. Iwata, Y. Hu, Battery Magnetometry Data 2019-2020. Open Science Framework. <https://osf.io/cw8zv/>. Deposited 27 February 2020.